

Electronic Supporting Information

A Lithium Difluorophosphate LiPO_2F_2 with a Neutral Polytetrahedral Microporous Architecture

Guopeng Han,^{a,b,†} Ying Wang,^{a,†} Hao Li,^{a,b} Zhihua Yang,^a and Shilie Pan^{*a}

^aCAS Key Laboratory of Functional Materials and Devices for Special Environments, Xinjiang Technical Institute of Physics & Chemistry, CAS; Xinjiang Key Laboratory of Electronic Information Materials and Devices, 40-1 South Beijing Road, Urumqi 830011, China.

^bCenter of Materials Science and Optoelectronics Engineering, University of Chinese Academy of Sciences, Beijing 100049, China

*To whom correspondence should be addressed.

†These authors contributed equally to this work.

Email: slpan@ms.xjb.ac.cn

Phone: (+86)991-3674558, Fax: (+86)991-3838957

Experimental Procedures

Reagents.

Lithium fluoride (LiF, 99.0 %), Phosphorus pentoxide (P_2O_5 , 99.99%), and Hexafluorophosphoric acid solution (HPF₆, ~60 wt. % in H₂O) were purchased from Aladdin Chemical Industry Co., Ltd. All chemicals used were of analytical grade and were used as received without any further purification.

Synthesis.

CAUTION: Hot autoclave is extremely hazardous and should be handled with the utmost care. Also, the reaction may produce HF gas as a side product, which is toxic by inhalation or in contact with skin when the cooled autoclave was opened.

LiPO₂F₂ was hydrothermally synthesized by reactions of a mixture of LiF, P₂O₅, and HPF₆. A total of 2.752 g of LiF, 5.678 g of P₂O₅, and 5 ml of HPF₆ was put into a 75 mL Teflon-lined autoclave. After stirring the mixture, the container was closed, heated at 220 °C for the following 2 h and held at this temperature for 5 days, and then cooled to room temperature at a cooling rate of 2 °C/h. After the reaction, the millimeter-level crystals of LiPO₂F₂ were obtained. The purity of the prepared sample was verified by powder X-ray diffraction (XRD). The product was then recrystallized in autoclave conditions with the same heating profile, and the colorless centimeter size block-shaped crystals of LiPO₂F₂ were harvested.

Characterization.

A suitable crystal was selected and mounted on a Bruker SMART APEX II 4K CCD diffractometer equipped with Mo K α radiation ($\lambda = 0.71073 \text{ \AA}$), and the diffraction data were collected at room temperature. Data integration, cell refinement and absorption corrections were carried out with the program SAINT.¹ Using Olex2,² the structure was solved with the ShelXT³ structure solution program using Intrinsic Phasing and refined with the ShelXL⁴ refinement package using Least Squares minimization. The structures were examined using the *Addsym* subroutine of PLATON,⁵ and no additional symmetry could be applied to the models. Crystallographic data and structural refinements for the title compound are summarized in Table S1. The final refined atomic positions and isotropic thermal parameters of each atom are illustrated in Table S2. Selected bond distances and angles are given in Table S3.

Powder XRD measurements of the LiPO₂F₂ sample was carried out using a Bruker D2 PHASER diffractometer equipped with an incident beam monochromator set for Cu K α radiation ($\lambda = 1.5418 \text{ \AA}$). Data were collected in the 2θ range of 10–70° with a scan step width of 0.02° and a fixed counting time of 1 s/step.

Elemental analysis was carried on a clean single crystal surfaces with the aid of a field emission scanning electron microscope (SUPRA 55VP) equipped with an energy dispersive X-ray spectroscopy (BRUKER x-flash-sdd-5010).

Thermal gravimetric (TG) and differential scanning calorimetry (DSC) were carried out on a simultaneous NETZSCH STA 449 F3 thermal analyzer instrument in a flowing N₂ atmosphere, the sample was placed in Pt crucible, heated from 40 to 750 °C at a rate of 5 °C min⁻¹.

The ultraviolet–visible–near-infrared transmittance spectrum was measured at room temperature on a single-crystal plate of LiPO₂F₂ with a thickness of 0.5 mm without polishing.

Infrared spectrum was recorded with a Shimadzu IR Affinity-1 Fourier transform infrared spectrometer in the range of 400–4000 cm⁻¹ with a resolution of 4 cm⁻¹.

Nitrogen adsorption/desorption isotherms were recorded at 77 K with a Quadachrome adsorption instrument. The sample is taken directly from the autoclave without grinding. Before analysis, the samples of millimeter single crystal of LiPO₂F₂ were degassed at 120 °C for 24 h. The surface area was calculated according to the Brunauer-Emmett-Teller (BET) method.

Computational Details.

The electronic structures of LiPO_2F_2 were performed using CASTEP package⁶ with the norm-conserving pseudopotentials (NCP)⁷, which is based on the plane-wave pseudopotential density functional theory. The Broyden–Fletcher–Goldfarb–Shanno (BFGS) minimization technique⁸ was employed in geometry optimization during the calculation and the converged criteria are that the residual forces on the atoms, the displacements and the energy change of atoms are less than 0.01 eV /Å, 5×10^{-4} Å and 5.0×10^{-6} eV respectively. The exchange and correlation energies are approximated within the generalized-gradient approximation (GGA)⁹ of the Perdew-Burke-Ernzerhof (PBE) formula. The plane-wave energy cutoff was set at 940.0 eV, and the Brillouin zone comprised $2 \times 2 \times 2$ with a separation of Monkhorst-Pack k-point sampling of 0.07/Å. The valence electrons of the elements in LiPO_2F_2 were calculated as follows: Li: $2s^1$, O: $2s^2 2p^4$, F: $2s^2 sp^5$, and P: $3s^2 3p^3$, respectively. The default values of the CASTEP code were retained for other parameters and convergent criteria.

For realizing a more accurate description of Eg for LiPO_2F_2 , the Heyd-Scuseria-Ernzerhof (HSE06) hybrid DFT functional as below was performed using the PWmat code¹⁰, which runs on graphics processing unit processors (GPU). NCPP-SG15-PBE pseudopotential¹¹ and 50 Ryd plane wave cutoff were used in all of our calculations.

$$E_{XC}^{HSE} = \alpha E_X^{HF,SR}(\mu) + (1 - \alpha) E_X^{PBE,SR}(\mu) + E_X^{PBE,LR}(\mu) + E_C^{PBE}$$

Where α is the mixing parameter and μ is an adjustable parameter controlling the short-range of the interaction.

Standard values of $\alpha = 0.25$ and $\mu = 0.2$ $E_X^{HF,SR}$ are the short range Hartree–Fock exact exchange functional, $E_X^{PBE,SR}(\mu)$ and $E_X^{PBE,LR}(\mu)$ are the short and long range components of the PBE exchange functional, and E_C^{PBE} is the PBE correlation functional. According to above equation, when the value of α varies from 0 to 100%, the form of exchange functional is changed from the pure PBE to pure HF, and correspondingly Eg increases gradually¹². In order to get a more reliable simulated result, an appropriate value of α needs to be confirmed. BPO_4 , a famous deep-ultraviolet optical crystal was selected as benchmark to preformed the DFT calculation caused by its large band gap and polytetrahedral architecture, which is similar to that of LiPO_2F_2 . The calculated band gap value of BPO_4 (9.545 eV) using $\alpha = 0.279$ is consistent well with the experimental value (9.544 eV). In this work, we use the same α to simulate the band gap of LiPO_2F_2 .

Table S1. Crystal data and structure refinement for LiPO₂F₂.

Empirical formula	LiPO ₂ F ₂
Formula weight	107.91
Wavelength (Å)	0.71073
Temperature (K)	296.15
Crystal system, space group	Monoclinic, C2/c
<i>a</i> / Å	9.672(8)
<i>b</i> / Å	19.310(15)
<i>c</i> / Å	8.055(6)
β / °	108.567(8)
Volume / Å ³	1426.0(19)
Z, Calculated density / g cm ⁻³	16, 2.011
Absorption coefficient / mm ⁻¹	0.651
<i>F</i> (000)	832.0
Crystal size / mm ³	0.123×0.106×0.074
Theta range for data collection	2.11 to 27.40
Limiting indices	-10 ≤ <i>h</i> ≤ 12, -21 ≤ <i>k</i> ≤ 24, -10 ≤ <i>l</i> ≤ 7
Reflections collected / unique	4295 / 1618 [<i>R</i> _{int} = 0.0263]
Completeness	99.3 %
Data / restraints / parameters	1618 / 0 / 111
Goodness-of-fit on <i>F</i> ²	1.048
Final <i>R</i> indices [<i>F</i> _o ² > 2σ(<i>F</i> _o ²)] ^[a]	<i>R</i> ₁ = 0.0482, <i>wR</i> ₂ = 0.1314
<i>R</i> indices (all data) ^[a]	<i>R</i> ₁ = 0.0730, <i>wR</i> ₂ = 0.1535
Largest diff. peak and hole / e·Å ⁻³	0.54 / -0.47

^[a]*R*₁ = $\sum ||F_o| - |F_c|| / \sum |F_o|$ and *wR*₂ = $[\sum w(F_o^2 - F_c^2)^2 / \sum wF_o^4]^{1/2}$ for *F*_o² > 2σ(*F*_o²)

Table S2. Wyckoff positions, site occupancy factors (S.O.F.), atomic coordinates ($\times 10^4$) and equivalent isotropic displacement parameters ($\text{\AA}^2 \times 10^3$) for LiPO_2F_2 .

Atoms	Wyck	S.O.F	x	y	z	* $U_{(\text{eq})}$	BVS
Li1	8f	1	3151(5)	6882(2)	5019(6)	36.7(11)	1.100
Li2	8f	1	4325(6)	4373(2)	9761(6)	39.4(12)	1.107
P1	4e	2	5000	8102.5(5)	7500	37.5(4)	5.172
P2	8f	1	2636.2(9)	5631.6(4)	7397.6(11)	40.0(3)	5.157
P3	4e	2	5000	3121.7(6)	7500	46.5(4)	5.287
O1	8f	1	3769(2)	7727.4(9)	6302(2)	37.4(5)	-2.061
O2	8f	1	3067(2)	5996.5(10)	6039(3)	41.2(6)	-2.055
O3	8f	1	3757(2)	5273.9(10)	8799(3)	44.9(6)	-2.064
O4	8f	1	4360(3)	3490.7(10)	8663(3)	44.4(6)	-2.064
F1	8f	1	4414(3)	8611.2(13)	8543(3)	102.8(10)	-1.070
F2	8f	1	1815(3)	6131.3(14)	8185(4)	100.2(10)	-1.079
F3	8f	1	1439(3)	5119.3(14)	6542(3)	100.4(10)	-1.079
F4	8f	1	6097(4)	2611.5(16)	8550(5)	148.7(16)	-1.123

* $U_{(\text{eq})}$ is defined as one third of the trace of the orthogonalized U_{ij} tensor (standard deviations in parentheses).

Table S3. Selected bond lengths (Å) and angles (°) for LiPO₂F₂.

Li1#2-O1	1.973(5)	P2-F2	1.512(2)
Li1-O1	1.922(5)	P2-F3	1.515(2)
Li1-O2	1.910(5)	P2-O2	1.512(2)
Li1#6-O4	1.973(5)	P2-O3	1.465(2)
Li2#4-O2	1.962(6)	P3-F4#1	1.497(3)
Li2#5-O3	1.969(6)	P3-F4	1.497(3)
Li2-O3	1.912(5)	P3-O4	1.462(2)
Li2-O4	1.926(5)	P3-O4#1	1.462(2)
P1-F1#1	1.515(2)		
P1-F1	1.515(2)		
P1-O1	1.464(2)		
P1-O1#1	1.464(2)		
O1-Li1-O3#3	92.5(2)	F2-P2-F3	100.4(2)
O1#3-Li1-O4	117.6(3)	O2-P2-F2	108.53(14)
O1-Li1-O5	118.0(3)	O2-P2-F3	109.37(15)
O2-Li1-O1	125.3(3)	O3-P2-F2	109.67(15)
O2-Li1-O1#3	114.4(3)	O3-P2-F3	108.31(15)
O2-Li1-O4#5	91.5(2)	O3-P2-O2	118.95(15)
O2#6-Li2-O3#4	116.2(3)	F4-P3-F4#1	97.7(4)
O3-Li2-O2#6	113.4(3)	O4#1-P3-F4	108.31(16)
O3-Li2-O3#4	91.1(2)	O4-P3-F4#1	108.31(16)
O3-Li2-O4	131.6(3)	O4#1-P3-F4#1	109.11(16)
O4-Li2-O2#6	91.3(2)	O4-P3-F4	109.12(16)
O4-Li2-O3#4	115.2(3)	O4#1-P3-O4	121.67(18)
F1-P1-F1#1	99.2(3)		
O1#1-P1-F1#1	108.47(14)		
O1#1-P1-F1	108.96(14)		
O1-P1-F1#1	108.96(14)		
O1-P1-F1	108.47(14)		
O1#1-P1-O1	120.67(17)		

Symmetry transformations used to generate equivalent atoms:

#1 1-X,+Y,3/2-Z; #2 1/2+X,3/2-Y,1/2+Z; #3 1/2-X,3/2-Y,1-Z; #4 1-X,1-Y,2-Z; #5 +X,1-Y,-1/2+Z;
#6 +X,1-Y,1/2+Z; #7 1-X,1-Y,1-Z.



Figure S1. Photographs of the as-grown crystals of LiPO₂F₂.

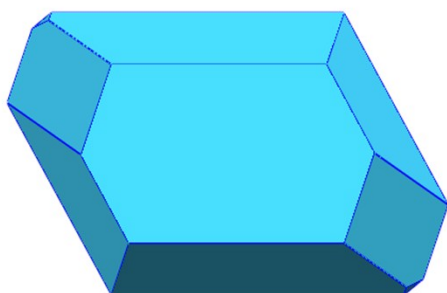


Figure S2. a) Observed theoretical morphology of LiPO₂F₂; (b) Photographic micrograph of LiPO₂F₂ by spontaneous crystallization.

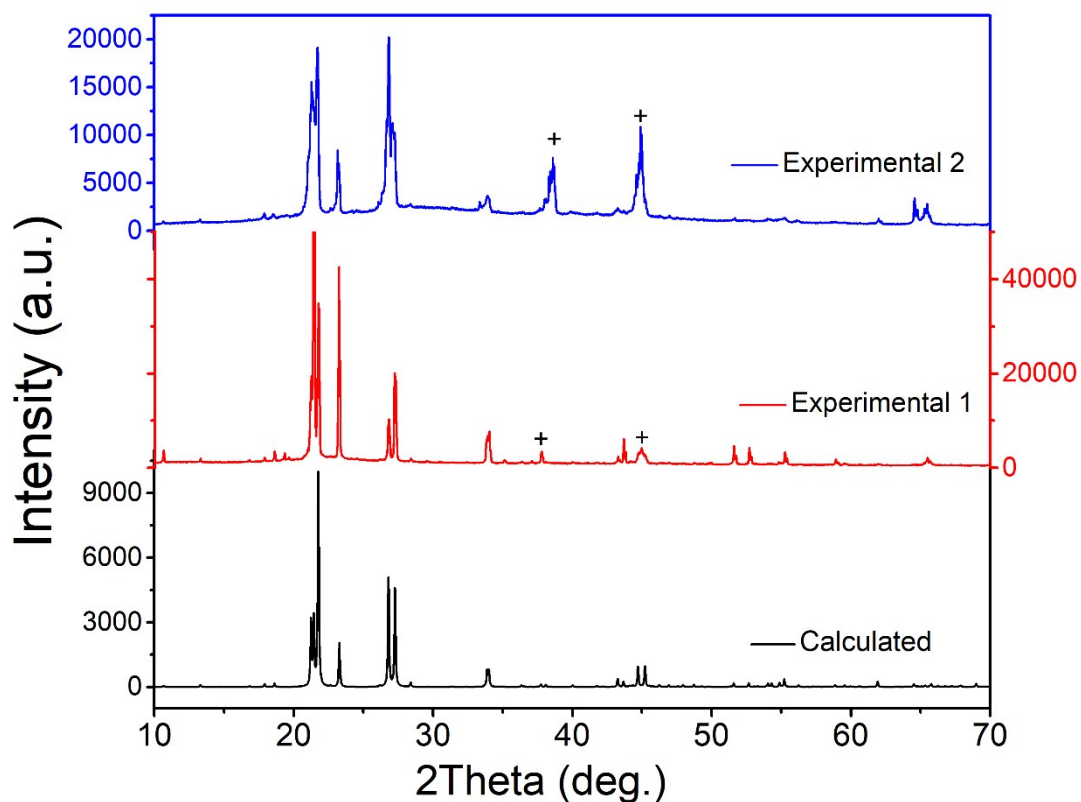
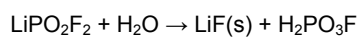


Figure S3. The calculated and experimental powder XRD patterns of LiPO_2F_2 . The sample is taken directly from the autoclave. The reflections marked with a black cross stem from LiF (PDF# 04-0857). The powder XRD pattern of experimental 1 is obtained from the sample after coarse grinding. The pattern of experimental 2 is obtained from the sample after fine grinding. We can find that the discrepancy between experimental and calculated intensities in the powder XRD patterns would be reduced after fine grinding, which confirms that the discrepancy comes from the preferred orientation of the LiPO_2F_2 crystals. Besides, it is noted that fine grinding causes an increase of the diffraction peak intensity of LiF (marked with a black cross), which are probably due to the following decomposition reaction:



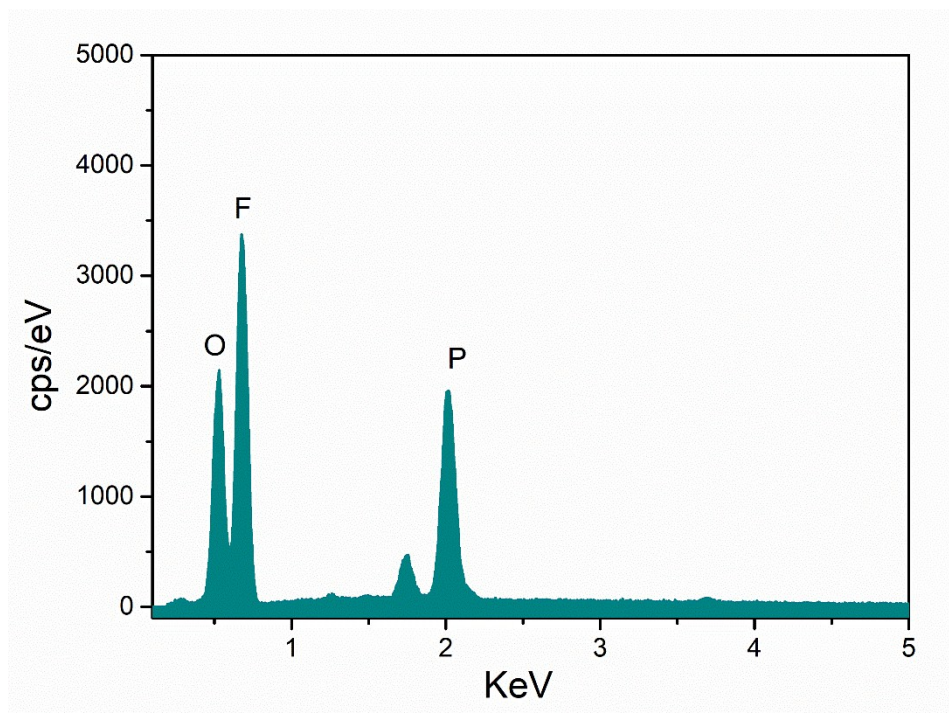


Figure S4. Elemental analysis. Energy dispersive X-ray spectroscopy confirms the existence of the fluorine element. Li cannot be detected by this technique because its emission lines lie below the lower detection limit of the system.

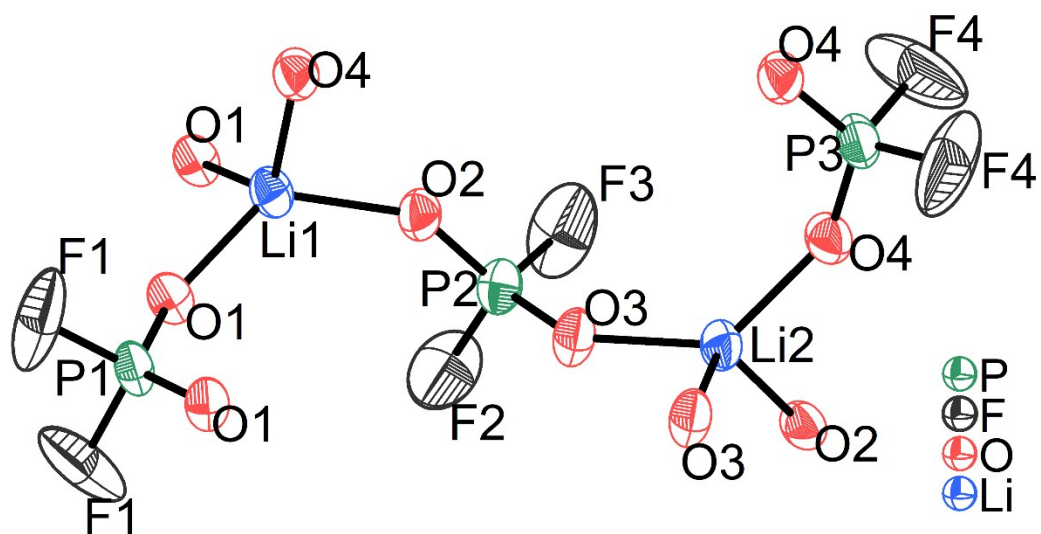


Figure S5. The asymmetric unit and symmetry-equivalent atoms of LiPO_2F_2 . Thermal ellipsoids are drawn at the 50% probability level.

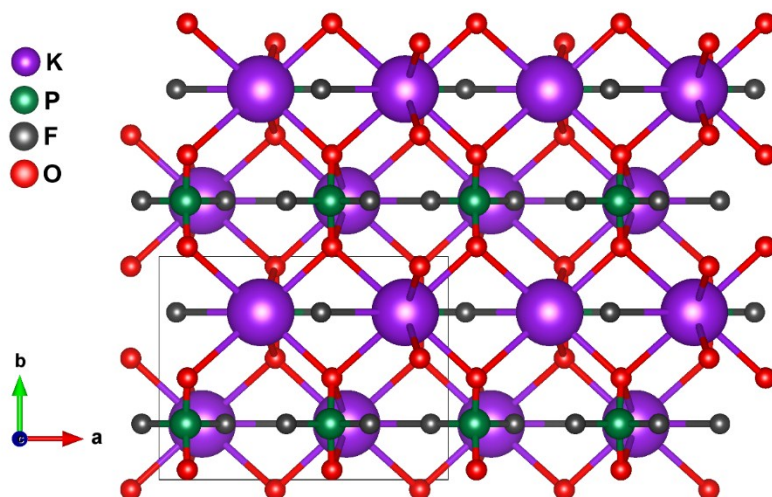


Figure S6. The structure of KPO₂F₂.

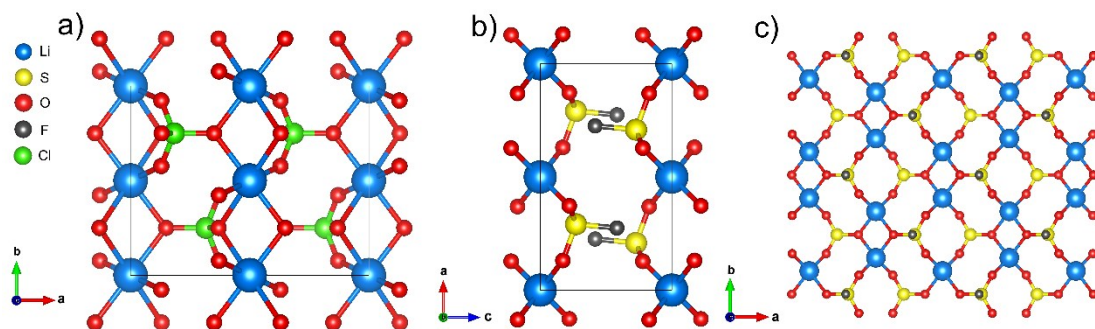


Figure S7. The structures of a) LiClO₄ and b) LiSO₃F and c) a 2D infinite layer of LiSO₃F.

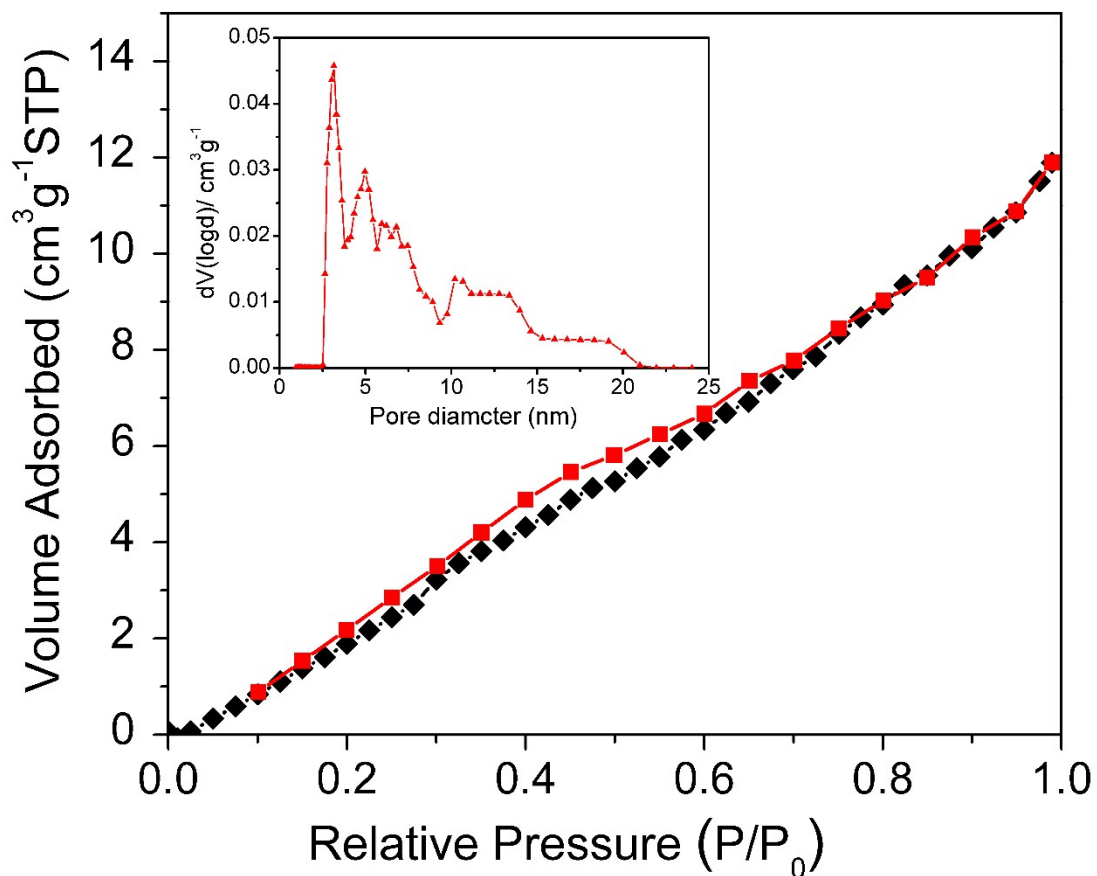


Figure S8. N₂ adsorption/desorption isotherms and pore size distribution of block crystal of LiPO₂F₂. The sample is taken directly from the autoclave without grinding. The N₂ quantity adsorbed by each adsorbent gradually increases with increasing relative pressure (P/P₀). The specific surface area is 38.6 m²g⁻¹ and the average pore wideness is 3.2 nm.

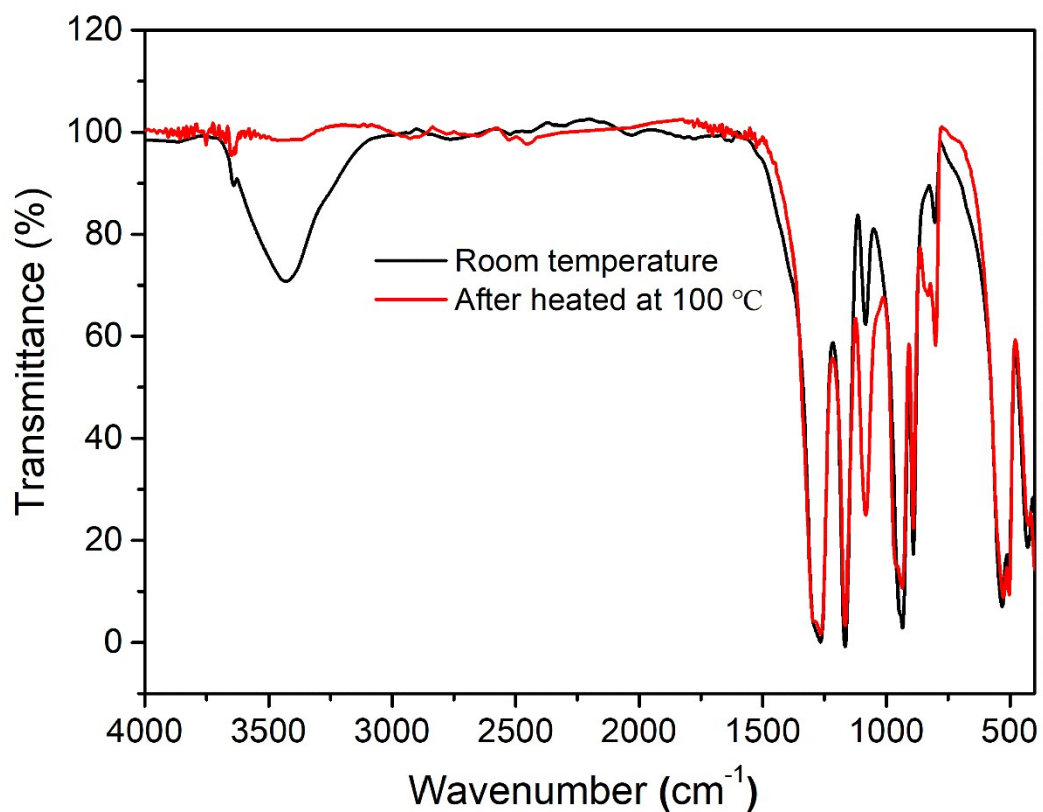
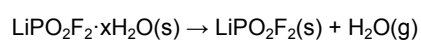


Figure S9. IR spectra I (black solid line) and II (red solid line) of LiPO₂F₂. IR spectrum I is performed with the sample directly from the autoclave. The IR spectrum II is measured with the sample after heated at 100 °C for 24 h. The significant difference between I and II is that the former shows the typical broad band of water caused by the hygroscopy of as-synthesized sample. The broad band between 3700 – 3000 cm⁻¹ are removed in the IR spectrum II, as described by below reaction:



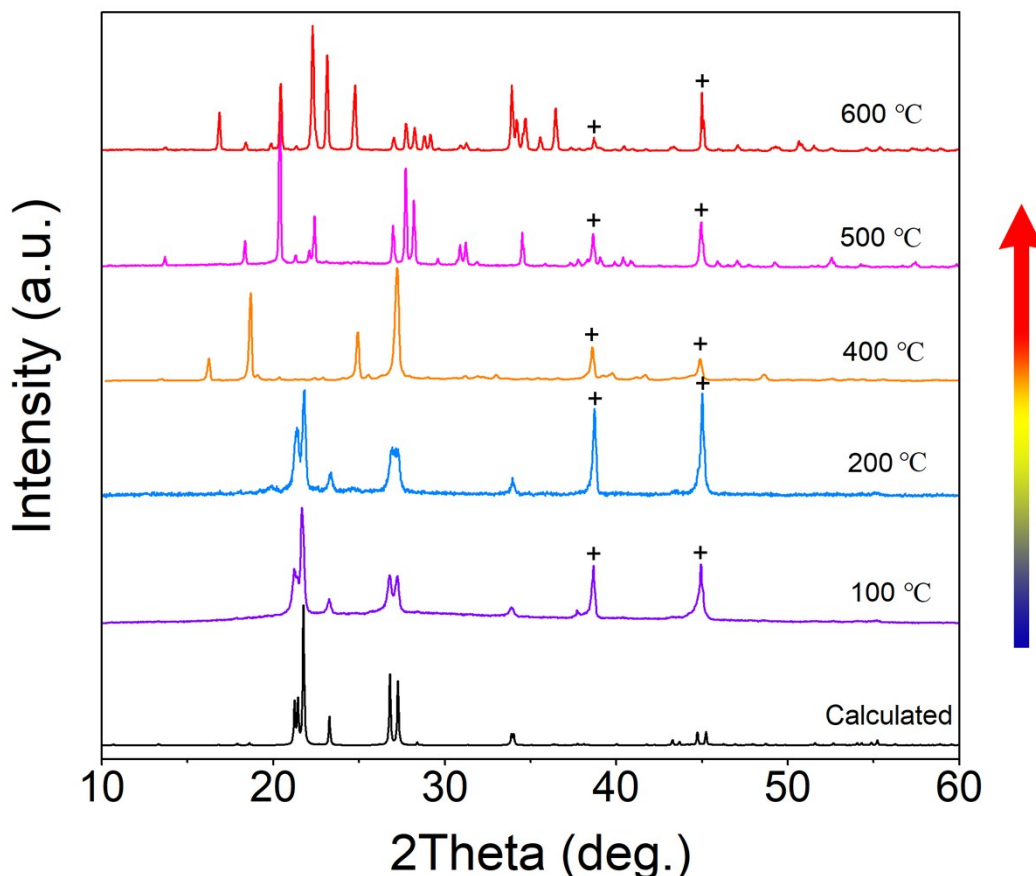


Figure S10. The powder XRD patterns of LiPO_2F_2 and its thermal decomposition products at 100, 200, 400, 500 and 600 °C for 10 h, respectively. The sample was heated subsequently at various temperatures in the same batch in air. The arrow on the right-hand side shows the temporal course of the experiment. The reflections marked with a black cross stem from LiF (PDF# 04-0857).

The decomposition reactions of $4\text{LiPO}_3 \rightarrow \text{Li}_4\text{P}_2\text{O}_7 + \text{P}_2\text{O}_5$ and $3\text{Li}_4\text{P}_2\text{O}_7 \rightarrow 4\text{Li}_3\text{PO}_4 + \text{P}_2\text{O}_5$ are consistently during the heating process, which have been well confirmed by powder XRD. However, the sequence of formation of LiPO_3 (PDF# 26-1177), $\text{Li}_4\text{P}_2\text{O}_7$ (PDF# 13-0440), and Li_3PO_4 (PDF# 15-0760) with rising temperature is not just thermal release of $\text{P}_4\text{O}_{10}(\text{g})$, since the meta- and pyrophosphates show higher thermal stabilities. Therefore, the decomposition steps of LiPO_2F_2 are very likely to be described by the subsequent reactions:

- (1) $\text{LiPO}_2\text{F}_2 \cdot x\text{H}_2\text{O}(\text{s}) \rightarrow \text{LiPO}_2\text{F}_2(\text{s}) + x\text{H}_2\text{O}(\text{g})$
- (2) $\text{LiPO}_2\text{F}_2(\text{s}) + \text{H}_2\text{O}(\text{g}) \rightarrow \text{LiF}(\text{s}) + \text{H}_2\text{PO}_3\text{F}$
- (3) $\text{LiPO}_2\text{F}_2(\text{s}) \rightarrow 1/2 \text{LiPO}_3(\text{s}) + 1/2 \text{LiF}(\text{s}) + 1/2 \text{POF}_3(\text{g})$
- (4) $\text{LiPO}_2\text{F}_2(\text{s}) \rightarrow 1/5 \text{Li}_4\text{P}_2\text{O}_7(\text{s}) + 1/5 \text{LiF}(\text{s}) + 3/5 \text{POF}_3(\text{g})$
- (5) $\text{LiPO}_2\text{F}_2(\text{s}) \rightarrow 1/3 \text{Li}_3\text{PO}_4(\text{s}) + 2/3 \text{POF}_3(\text{g})$

The title compound is hygroscopic, and the water could be removed when heated in air, as described by reaction (1). The XRD patterns at 100 and 200 °C consist of two phases: $\text{LiPO}_2\text{F}_2(\text{s})$ and $\text{LiF}(\text{s})$. The formation of LiF might well be understood by reaction (2), where $\text{H}_2\text{PO}_3\text{F}$ would further decompose according to the following equation: $3\text{H}_2\text{PO}_3\text{F} \rightarrow 2\text{H}_3\text{PO}_4 + \text{POF}_3$. The XRD pattern at 400 °C consists of two phases: $\text{LiPO}_3(\text{s})$ and $\text{LiF}(\text{s})$, which can be described by reaction (3). The XRD pattern at 500 °C consists of two phases: $\text{Li}_4\text{P}_2\text{O}_7(\text{s})$ and $\text{LiF}(\text{s})$, which can be described by reaction (4). The XRD pattern at 600 °C mainly consists of two phase:

$\text{Li}_3\text{PO}_4(\text{s})$ and $\text{Li}_4\text{P}_2\text{O}_7(\text{s})$, which can be described by reactions (4) and (5). It is worth mentioning that the reactions from (3) to (5) have the strong temperature dependence.

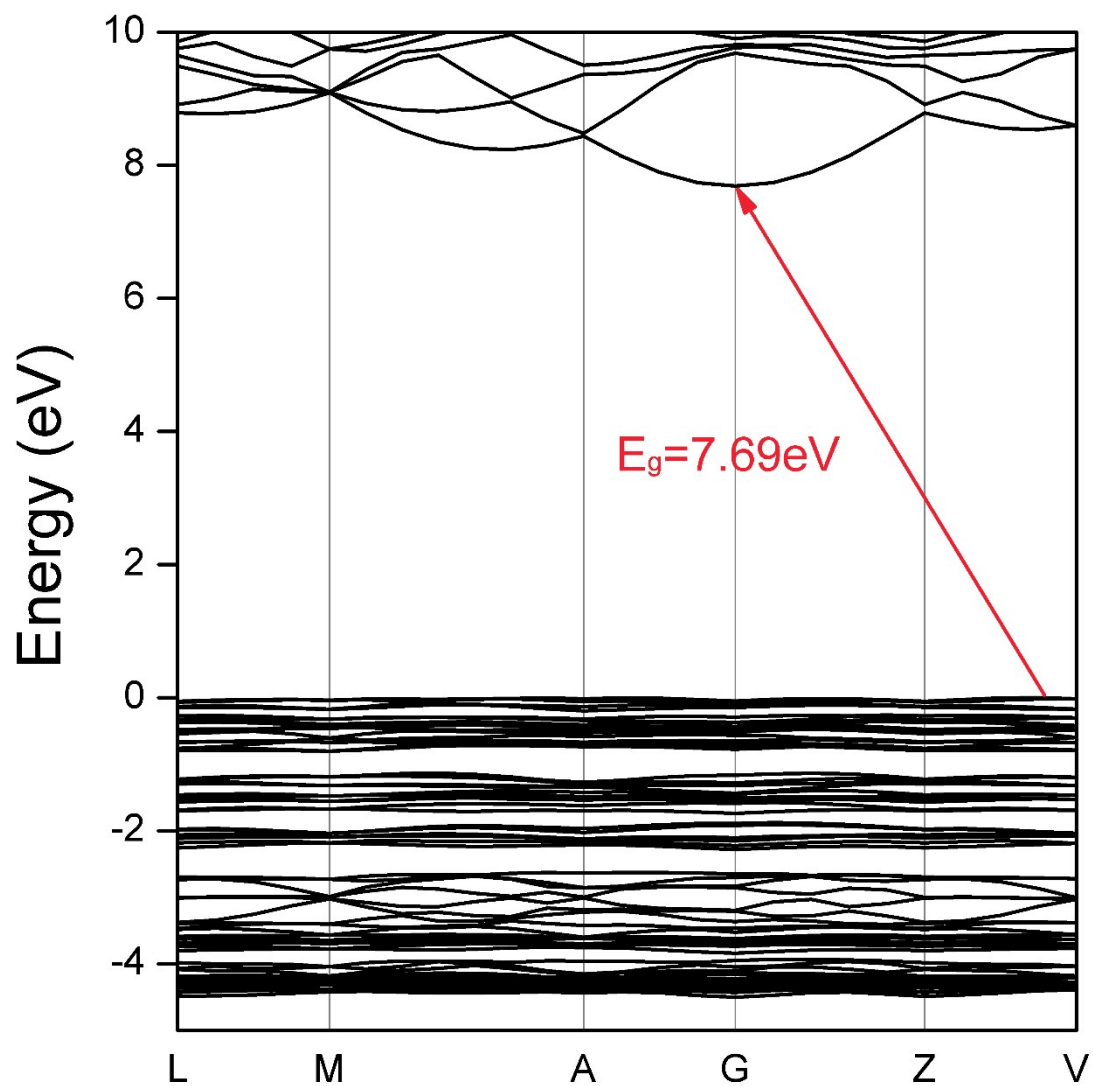


Figure S11. Electron band structures of LiPO_2F_2 . The arrow indicates the indirect bandgap.

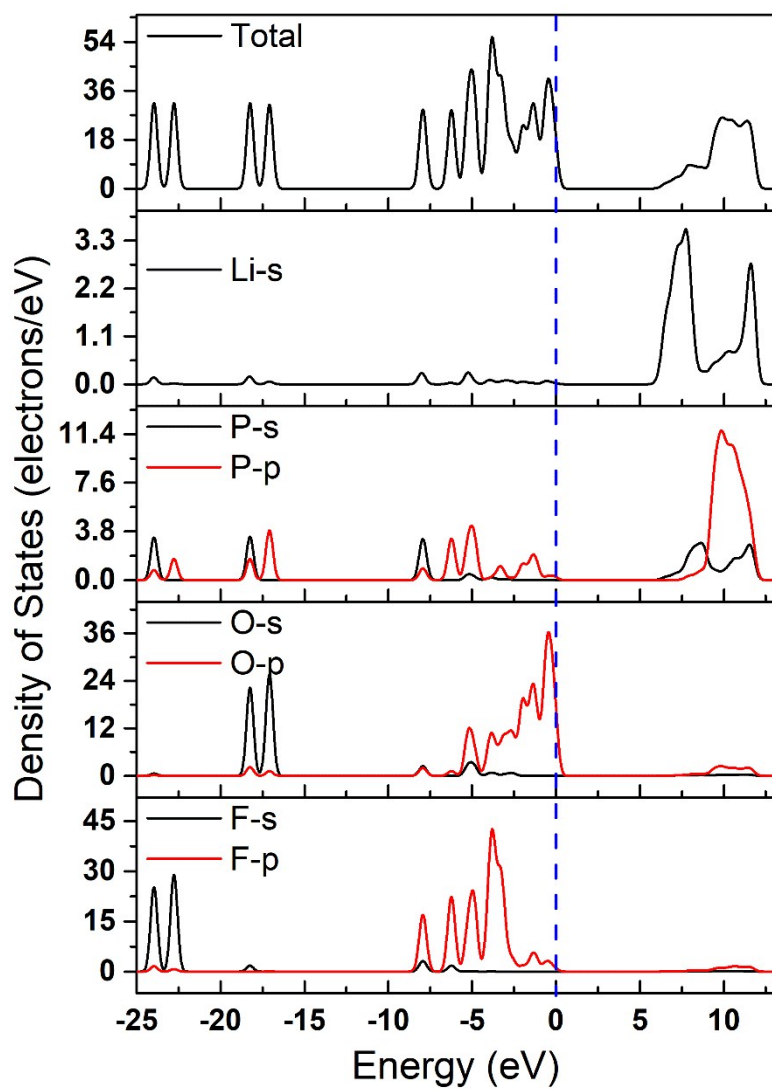


Figure S12. The density of states of LiPO_2F_2 .

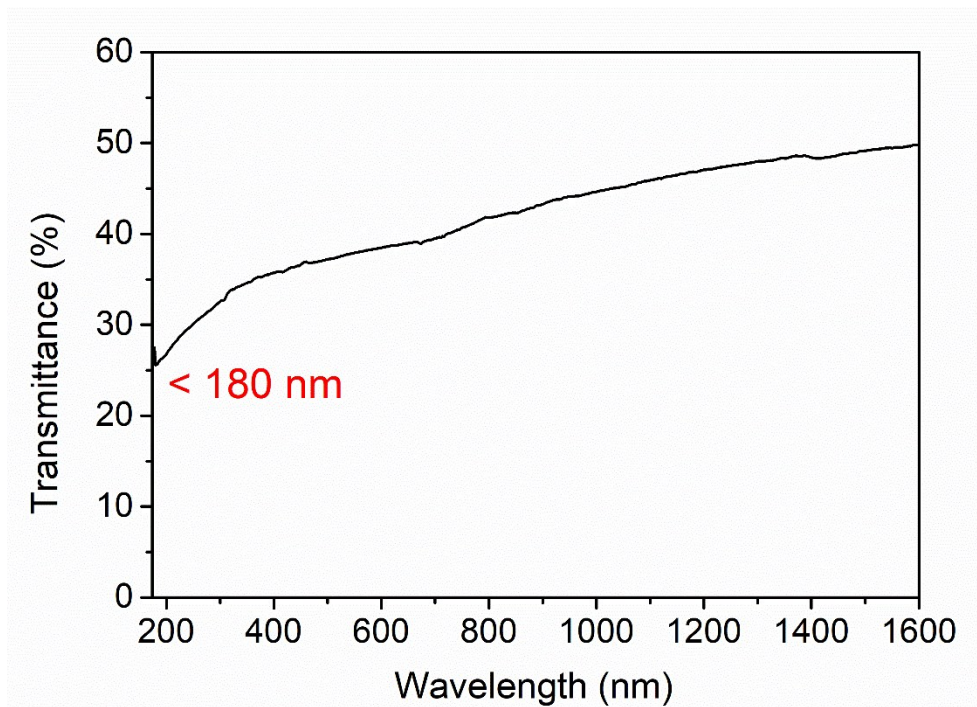


Figure S13. The ultraviolet-visible-near-infrared transmittance spectrum of LiPO₂F₂.

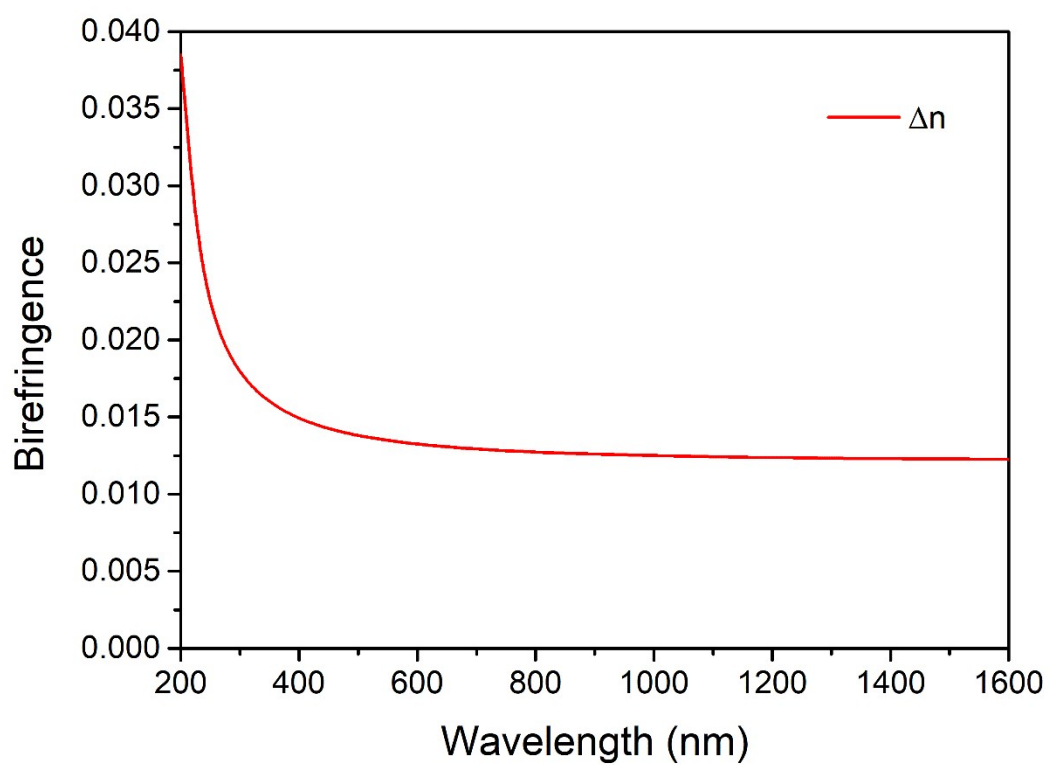


Figure S14. Calculated birefringence dispersion curve for LiPO_2F_2 .

References

1. *SAINT, Version 7.60A*, Bruker Analytical X-ray Instruments, Inc., Madison, WI, 2008.
2. O. V. Dolomanov, L. J. Bourhis, R. J. Gildea, J. A. K. Howard and H. Puschmann, *J. Appl. Cryst.*, 2009, **42**, 339-341.
3. G. M. Sheldrick, *Acta Crystallogr.*, 2015, **A71**, 3-8.
4. G. M. Sheldrick, *Acta Crystallogr.*, 2015, **C71**, 3-8.
5. A. Spek, *J. Appl. Crystallogr.*, 2003, **36**, 7-13.
6. S. J. Clark, M. D. Segall, C. J. Pickard, P. J. Hasnip, M. I. Probert, K. Refson and M. C. Payne, *Z. Kristallogr. - Cryst. Mater.*, 2005, **220**, 567-570.
7. (a) A. M. Rappe, K. M. Rabe, E. Kaxiras and J. D. Joannopoulos, *Phys. Rev. B*, 1990, **41**, 1227-1230; (b) J. S. Lin, A. Qteish, M. C. Payne and V. Heine, *Phys. Rev. B*, 1993, **47**, 4174-4180; (c) M.-H. Lee, Ph.D, The University of Cambridge, 1996.
8. B. G. Pfrommer, M. Côté, S. G. Louie and M. L. Cohen, *J. Comput. Phys.*, 1997, **131**, 233-240.
9. J. P. Perdew, K. Burke and M. Ernzerhof, *Phys. Rev. Lett.*, 1996, **77**, 3865.
10. (a) W. Jia, Z. Cao, L. Wang, J. Fu, X. Chi, W. Gao and L.-W. Wang, *Comput. Phys. Commun.*, 2013, **184**, 9-18; (b) W. Jia, J. Fu, Z. Cao, L. Wang, X. Chi, W. Gao and L.-W. Wang, *J. Comput. Phys.*, 2013, **251**, 102-115.
11. (a) M. Schlipf and F. Gygi, *Comput. Phys. Commun.*, 2015, **196**, 36-44; (b) D. R. Hamann, *Phys. Rev. B*, 2013, **88**, 085117.
12. (a) I. de P. R. Moreira, F. Illas and R. L. Martin, *Phys. Rev. B*, 2002, **65**, 155102; (b) Y.-f. Zhang, W. Lin, Y. Li, K.-n. Ding and J.-q. Li, *J. Chem. Phys. B*, 2005, **109**, 19270-19277.